frontiers | Frontiers in Astronomy and Space Sciences

TYPE Original Research
PUBLISHED 30 April 2024
DOI 10.3389/fspas.2024.1369368

OPEN ACCESS

EDITED BY
Shangqing Yang,
Huazhong University of Science and Technology, China

REVIEWED BY
Debi Prasad Choudhary,
California State University, United States
Victor De La Luz,
National Autonomous University of Mexico, Mexico

*CORRESPONDENCE
Changhui Rao,
chrao@ioe.ac.cn

RECEIVED 12 January 2024
ACCEPTED 08 April 2024
PUBLISHED 30 April 2024

CITATION
Rao C, Ji H, Bao H, Rao X, Yang J, Guo Y, Zhang L, Zhong L, Fan X, Zhang Q, Li C and Bian Q (2024), PASAT: pathfinder in solar adaptive telescope.
Front. Astron. Space Sci. 11:1369368.
doi: 10.3389/fspas.2024.1369368

PASAT: pathfinder in solar adaptive telescope

Changhui Rao[1,2,3]*, Haisheng Ji[3,4], Hua Bao[1,2], Xuejun Rao[1,2], Jinsheng Yang[1,2], Youming Guo[1,2], Lanqiang Zhang[1,2], Libo Zhong[1,2], Xinlong Fan[1,2], Qingmin Zhang[4], Cheng Li[1,2] and Qing Bian[1,2,3]

[1]National Laboratory on Adaptive Optics, Chengdu, Sichuan, China, [2]Institute of Optics and Electronics, Chinese Academy of Sciences, Chengdu, Sichuan, China, [3]School of Electronic, Electrical and Communication Engineering, University of Chinese Academy of Sciences, Beijing, China, [4]Purple Mountain Observatory, Chinese Academy of Sciences, Nanjing, China

In the forefront of quantitative solar physics research using large-aperture ground-based solar optical telescopes, high-contrast observation along with high-accuracy polarimetric measurement in the solar active region are required. In this paper, we propose a novel high-contrast imaging telescope construction with a 60 cm medium aperture, namely, the PAthfinder in Solar Adaptive Telescope (PASAT), in which a deformable secondary mirror is used as the adaptive optical correction device and a symmetrical optical path design is employed, leading to the least Muller matrix polarization instruments. The telescope can provide a high-resolution magnetic field with high accuracy for the solar active regions, as well as high-contrast images with a superior signal-to-noise ratio and photometric accuracy of the solar photosphere and chromosphere. These data will be directly used for a better understanding of the evolution and release of magnetic energy, which will help in improving space weather forecasting. Meanwhile, PASAT will accumulate the relevant techniques for constructing similar, larger solar telescopes in the future.

KEYWORDS

solar telescope, high resolution, adaptive optics, deformable secondary mirror, high contrast

1 Introduction

Solar activity is the source of space weather, and active bodies such as solar flares and coronal mass ejections are large-scale magnetic energy-releasing processes in the solar atmosphere. However, their energy accumulation and triggering are rooted in the chromosphere and photosphere and have smaller scales (Low, 2015; Wang et al., 2015; Choudhuri, 2017). Ground-based, large-aperture solar telescopes are still the best choice for studying the ultra-fine structure of solar active regions. Adaptive optical technology is also increasingly mature, which ensures the high-resolution observation of ground-based telescopes near the diffraction limit (Cao et al., 2010; Rimmele and Marino, 2011).

For solar observation, we not only need larger aperture telescopes to achieve higher spatial resolution and collect more photons, but we also need higher imaging contrast to achieve a higher detection signal-to-noise ratio and photometric accuracy. However, a prominent drawback of solar telescopes is the high scattered light, which makes the imaging contrast far from the requirements.

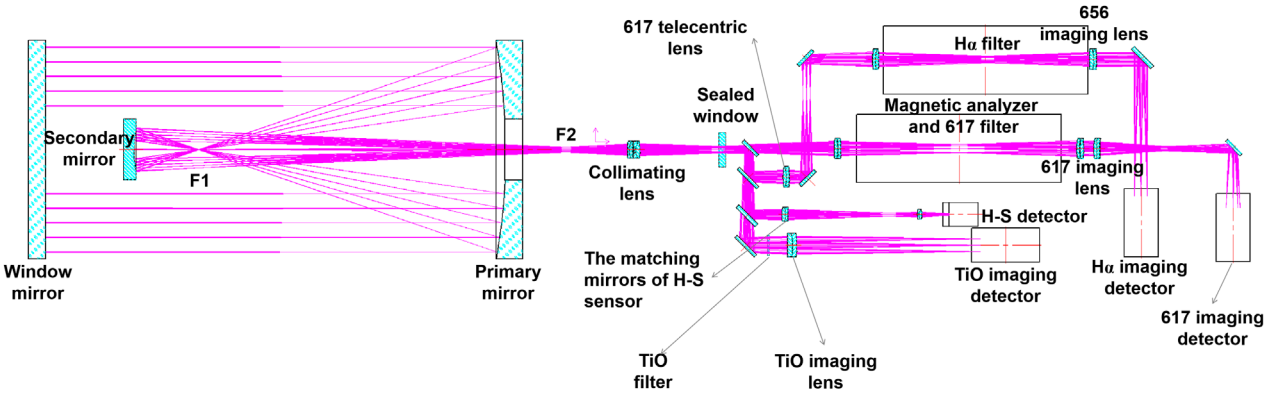

FIGURE 1
Optical configuration of PASAT.

The large-aperture ground-based solar telescopes that have been built internationally, such as the 1 m Swedish 1-m Solar Telescope (SST) (Scharmer et al., 2002), 1.5 m GREGOR (Schmidt et al., 2012; Schmidt et al., 2016; Kleint et al., 2020), 1.6 m Goode Solar Telescope (GST) (Rimmele et al., 2004; Cao et al., 2010; Shumko et al., 2014; Schmidt et al., 2017), 1 m New Vacuum Solar Telescope (NVST) (Liu et al., 2014), 1.8 m Chinese Large Solar Telescope (CLST) (Rao et al., 2020), 4 m Daniel K. Inouye Solar Telescope (DKIST) (Rimmele et al., 2020; Rast et al., 2021), and 2.5 m wide-field and high-resolution solar telescope (WeHoST) (Fang et al., 2019) under construction, are equipped with solar adaptive optical systems between the telescope and scientific terminal to correct atmospheric turbulence and the tracking and wavefront errors of the telescope itself. The optical path of this structural form is very complex, and there are also many optical mirrors for light passing through (taking the 1-meter new vacuum solar telescope as an example, a total of 21 optical mirrors are employed from the telescope to the back-end scientific instrument through an adaptive optics system). As a result, the spatial resolution of the obtained images can approach the optical diffraction limit, but the image contrast is severely limited.

In order to achieve high-contrast imaging of solar targets, it is necessary to strictly control the stray light of the system, as well as the wavefront residual error (especially high-frequency error) and non-common path aberration of the system, to achieve a high Strehl ratio (SR) of imaging. This article proposes using the deformable secondary mirror as an adaptive optical correction device, tightly coupling the telescope and adaptive optics, which can greatly simplify the optical path and significantly reduce the number of optical mirrors in the system, thereby reducing both the effects of stray light and the high-frequency wavefront aberration of the system. It is the best choice to achieve high-contrast solar target imaging. At the same time, the new solar adaptive telescope system has very high optical efficiency, which can reduce the exposure integration time of the imaging camera (especially for magnetic field measurement and limited imaging of weak light, such as the narrowband of the chromosphere), greatly improving the temporal resolution of telescope imaging. Therefore, the large-aperture solar adaptive telescope using a deformable secondary mirror can achieve continuous observation of solar targets with high contrast, high spatial resolution, and high temporal resolution simultaneously.

As good night vision and imaging occur in the infrared band, the deformable secondary mirror in a night astronomical telescope has low requirements for driver density. Due to the relatively poor daytime vision and imaging in the visible band, the deformable mirror requires a much higher driver density. Most of the night astronomical deformable secondary mirrors using voice-coil motors (Wildi et al., 2003; Esposito et al., 2011; Briguglio et al., 2013; Morzinski et al., 2014; Briguglio et al., 2018) have the disadvantage of large actuator spacing, leading to complex thermal control, and are not suitable for daytime solar applications. The piezoelectric deformable secondary mirror that we proposed can achieve high density and has low thermal radiation, making it especially suitable for high-contrast solar imaging applications. This deformable mirror with high driver density has been successfully tested on a night astronomical telescope and achieved high-contrast imaging with SR close to 0.5 in the 0.64 um wavelength band (Guo et al., 2016a; Guo et al., 2016b; Guo et al., 2023). In the field of solar observation, the 4 m European Solar Telescope (EST) (Soltau et al., 2010) is considered to use the deformable secondary mirror in multi-conjugate adaptive optics (MCAO) to carry out ground-layer corrections.

The solar adaptive telescope we proposed adopts our self-developed small-spacing and high-density piezoelectric deformable secondary mirror (PDSM). The optical components of the telescope and the adaptive optical system only consist of one primary mirror and one secondary mirror, making the optical path extremely simplified. It is particularly suitable for high-order correction of the wavefront disturbance induced by atmospheric turbulence, and it is very conducive to high-contrast imaging. Moreover, the optical path of the magnetic field measurement channel is completely symmetrical, and this will not introduce additional calibrations for polarization instruments, which can effectively improve the accuracy of the polarization measurement.

In this paper, the preliminary design of PASAT is introduced in Section 2. In Section 3, the key components are described, including the deformable secondary mirror, correlating Hartmann–Shack (HS) wavefront sensor, high-resolution photometric magnetism

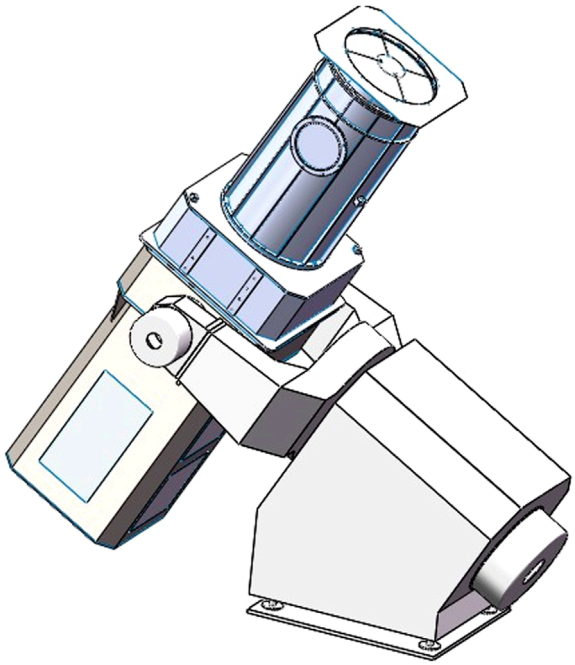

FIGURE 2
Overall structure diagram of the 60 cm solar adaptive telescope.

measurement, and high-resolution imaging systems. In Section 4, the system's performance is evaluated. Finally, we conclude the work in Section 5.

2 Preliminary optical design of PASAT

The optical configuration of PASAT, as shown in Figure 1, is composed of a 60 cm aperture primary mirror, a 163-element deformable secondary mirror, a correlating Hartmann–Shack wavefront sensor, a high-resolution photometric magnetism measurement at 617.3 nm, and two-channel high-resolution imaging systems at the Hα (656.28 nm) and TiO (705.8 nm) bands. The overall configuration of PASAT is shown in Figure 2. The vacuum tube for the primary optical system and the polar axis equatorial mount are used, and a thermal field stop and its active thermal control system are installed at the main focus F1 between the primary and secondary mirrors, which can reflect sunlight outside the imaging field of view from the optical system and effectively reduce the solar radiation power in the secondary mirror, relay optical components, and observation equipment. This technical solution has been successfully applied for the astronomical observation equipment of the Shanghai Astronomical Museum (Shanghai Science and Technology Museum Branch)—the Educational Adaptive Optics Solar Telescope (EAST) (Rao et al., 2022), which can ensure the stability of the optics of the instruments. The wavefront sensor and high-contrast imaging systems are fixed in the instrument box. The parameters of the primary mirror are clear aperture, 600 mm; vertex curvature radius, 1,800 mm; conic constant, K = 1.000; and central obscuration, 180 mm.

The main technical parameters of the PASAT are shown in Table 1.

TABLE 1 Main technical parameters of the telescope.

No	Parameter	Value
1	Effective clear aperture	φ600 mm
2	Field	φ8′
3	Wavelength	0.6 μm–0.71 μm
4	Magnetic-field measurement	Central wavelength: 617.3 nm/spectral bandwidth: 0.008 nm
5	Photosphere imaging	Central wavelength: 705.8 nm/spectral bandwidth: 0.1 nm
6	Chromosphere imaging	Central wavelength: 656.28 nm/spectral bandwidth: 0.025 nm
8	Imaging resolution	<0.3"@ 705.8 nm @ r0 (0.50 μm) = 6 cm
9	Strehl ratio	>0.7 @ r0 (0.50 μm) = 10 cm/>0.4 @ r0 (0.50 μm) = 6 cm
10	Polarization measurement accuracy	5 × 10E-4

3 Key components

3.1 Deformable secondary mirror

The 241-unit deformable secondary mirror has been successfully applied in the Lijiang 1.8 m night astronomical telescope system (Guo et al., 2023), which accumulated important technical experience for this project proposal. Referring to the 241-unit deformation secondary mirror experience of the Lijiang 1.8 m telescope, we conducted simulation calculations and design optimization on the actuator number and spatial layout of the deformation secondary mirror proposed in this project. We finalized that the PDSM actuators are arranged in a regular triangle configuration with a actuator spacing of 10.8 mm, and the total number of actuators is 163. The correction aperture is 130 mm, the central obscuration is 40 mm, and the single driver has a corrective stroke of ±3 μm. The arrangement of the PDSM actuators is shown in Figure 3. The influence function of the PDSM when driving an actuator is close to the Gaussian function, with a coupling of neighboring actuators of ~10.0% and a Gaussian index of ~2.2. The 241-unit deformation secondary mirror experience of the Lijiang 1.8 m telescope shows that the first 91 Zernike modes can be effectively corrected by this PDSM. The resonance frequency of the PDSM is larger than 4 kHz, and the error rejection bandwidth of the system would be mainly determined by the frame rate of the Hartmann–Shack wavefront senor. Table 2 lists the basic parameters of the PDSM design.

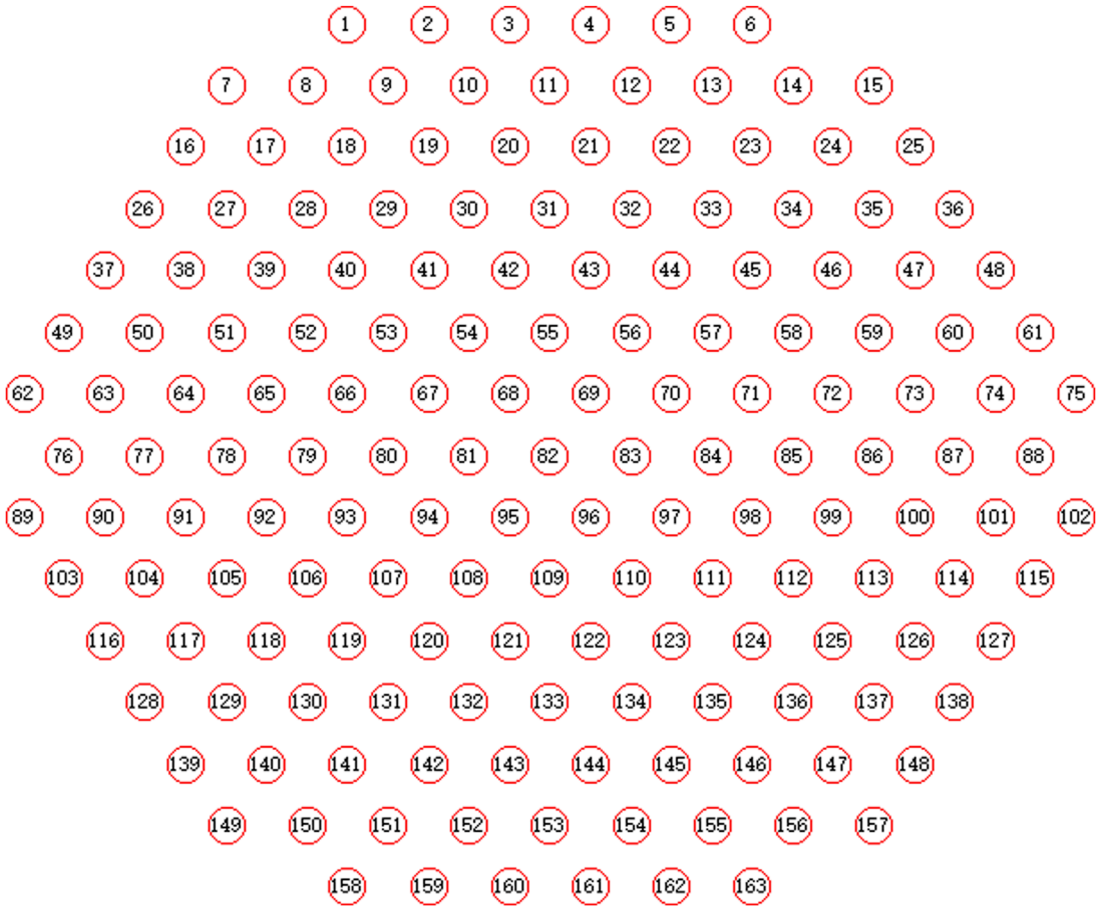

FIGURE 3
Arrangement of the PDSM actuators.

TABLE 2 Basic parameter requirements of high-density PDSM design.

No	Parameter	Value
1	Number of actuators	163
2	Arrangement pattern of actuators	regular triangle
3	Actuator spacing between actuators	10.80 mm
4	Clear aperture	130 mm
5	Vertex curvature radius	330.435 mm
6	Conic constant	−0.546
7	Estimated total mass	≈6 Kg

3.2 Correlating the Hartmann–Shack wavefront sensor

As one of the main components of the adaptive optics system, the performance of the wavefront sensor directly determines the final performance of the system. In solar adaptive optical systems, a Hartmann–Shack wavefront sensor based on the correlation algorithm is usually used. Our team has been conducting research on relevant wavefront sensors since 2009 (Rao et al., 2010) and has successfully developed correlating Hartmann–Shack wavefront sensors with sub-apertures ranging from 7 × 7 to 15 × 15 to 25 × 25. These wavefront sensors have successfully been applied in several solar adaptive optical systems, such as NVST (Rao et al., 2018; Zhang et al., 2023), EAST (Rao et al., 2022), and CLST (Rao et al., 2020), and have all achieved good wavefront detection results. In this project, we meet the requirements of small-field and high-order classic adaptive optics (CAO) correction and large-field and ground-layer ground-layer adaptive optics (GLAO) correction, and Figure 4 shows the layout diagrams of the two sub-apertures.

For the small-field and high-order CAO, the pixel resolution is initially determined to be 1.0"/pixel, with each sub-aperture corresponding to 24 × 24 pixels, and the corresponding detection field is approximately 24" × 24". The number of sub-aperture arrays is 15 × 15, the camera target surface is 360 × 360 pixels, and the camera frame rate can be more than 3,500 Hz. For the large-field and ground-layer GLAO, the maximum imaging area of the camera can reach more than 900 × 900 pixels under the condition that the wavefront detection frame rate is not less than 1,500 Hz.

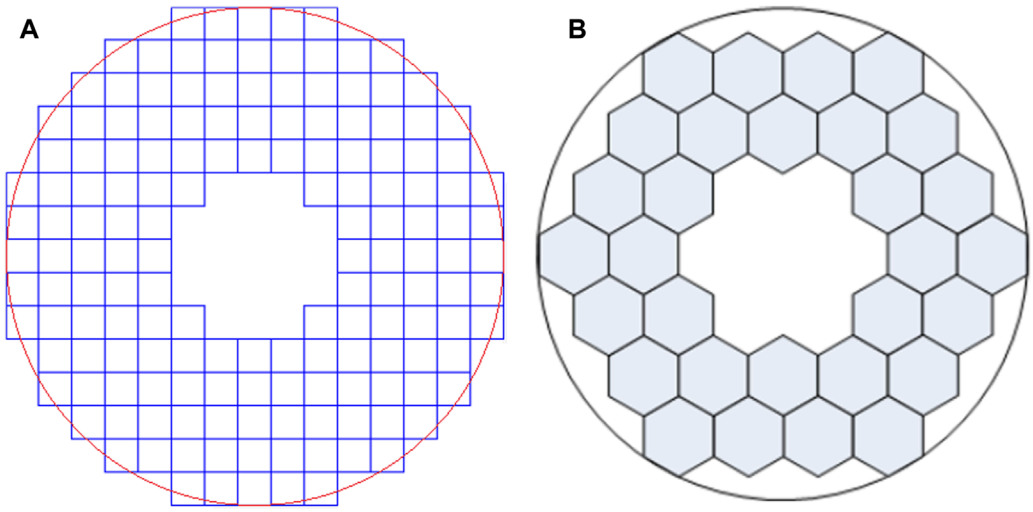

FIGURE 4
(A) Layout diagrams of small-field and high-order CAO sub-apertures; **(B)** layout diagrams of large-field and ground-layer GLAO sub-apertures.

TABLE 3 Main parameters of the Hartmann–Shack wavefront sensors.

Parameter type	Small-field and high-order	Large-field and ground-layer
Detection wavelength	600 nm–710 nm	600 nm–710 nm
Detection frame rate	≥3,500 Hz	≥1,500 Hz
Sub-aperture	15 × 15	7 × 7
Pixel resolution	~1.0"/pixel	~0.6"/pixel
Detection field	~24" × 24″	~74" × 85″
Number of guiding area	1	6–9

Combined with the detection speed of the camera and the previous experimental results of the adaptive optics (AO) system, the pixel resolution of the camera image is set as 0.6"/pixel, the number of sensor sub-aperture arrays is 7 × 7 so that each sub-aperture corresponds to 124 × 142 pixels, and the corresponding detection field is approximately 74" × 85". The main technical parameters of the Hartmann–Shack wavefront sensors are listed in Table 3.

3.3 High-resolution photometric magnetism measurement

The high-resolution magnetic field measurement subsystem is mainly composed of a pre-filter, imaging lens, polarization calibration unit, narrow-band filter, polarization analyzer, imaging camera, and magnetic field inversion unit.

The pre-filter is located at the front of the narrowband filter and is used to adjust the transmission wavelength of the filter. The specific requirements include the following: clear aperture ≥ 50 mm, central wavelength 617.3 nm, transmission spectral half-width of 2 nm, and transmission wavefront RMS ≤ 0.1λ.

The polarization analyzer has the following three types: mechanical rotation modulation based on the wave plates and polarizers, DKDP, and liquid crystal. In the first consideration, DKDP or the liquid crystal modulator is used.

The narrow-band filter adopts the scheme of a birefringent Lyot filter, which can achieve a transmission bandwidth narrower than the line width of the magneto-sensitive spectral line and can also contour scan the spectral lines by adjusting the central wavelength. The two-dimensional polarization spectral information of the Sun can be obtained through the combination of the polarization analyzer and the narrow-band adjustable filter, and thus, it inversely infers the two-dimensional magnetic field image of the Sun.

The basic parameter requirements of the magnetic field measurement system (including wavelength, polarization measurement accuracy, birefringent Lyot filter, and camera pixel count) are shown in Table 4.

3.4 High-resolution imaging systems

In this instrument, we selected two spectral lines, the Hα line and TiO line, which are commonly used for high-resolution

TABLE 4 Basic parameter requirements of the magnetic field measurement system.

No	Parameter	Value
1	Central wavelength	617.3 nm
2	Full width at half maximum (FHWM) of transmittance	≤0.008 nm
3	Shift range of the wavelength	±0.03 nm
4	Operating temperature	42°C ± 1°C
5	Aperture	≥40 mm
6	Polarization measurement accuracy	5 × 10E-4
7	Camera pixel count	4,096 × 4,096 pixels

TABLE 5 Parameters of the imaging optical system.

Parameter	High-resolution hα imaging	High-resolution TiO imaging
Wavelength	656.281 nm	705.8 nm
Bandwidth	0.025 mm	0.5 nm
FoV	56.5″	56.5″
Pixel resolution	0.106″	0.106″
Camera pixel count	4,096 × 4,096 pixels	4,096 × 4,096 pixels

TABLE 6 Analysis of the aberration correction results using the layout matching of deformable secondary mirror under different atmospheric coherence lengths (r0) conditions.

r0 (500 nm)	5 cm	8 cm	10 cm	12 cm	15 cm
Measurement error (nm)	44	30	25	21	17
Fitting error (nm)	41	28	23	20	16
Total error (nm)	60	41	34	29	24
Imaging SR (617 nm)	0.688	0.840	0.887	0.916	0.942
Imaging SR (656 nm)	0.719	0.857	0.899	0.926	0.949
Imaging SR (705 nm)	0.751	0.875	0.912	0.935	0.955

solar observation, to carry out high-contrast and high-resolution imaging observations of the solar active region. For high-resolution imaging at the Hα band, a scientific Lyot filter based on crystal birefringence will be used in the system, and the parameters of the high-resolution imaging optical system are shown in Table 5.

4 System performance evaluation

The closed-loop residual variance of the AO system is mainly composed of the measurement error of the HS sensors and the fitting error of PDSM (Hardy and Thompson, 2000), and we estimated the system performance based on the parameters of these two parts. The Strehl ratio of the 617 nm imaging system with the shortest wavelength is also better than 0.68 when r0 is only 5 cm, which ensures the high-contrast imaging of the solar target by this instrument. Table 6 shows the analysis of the aberration correction results using the layout matching of the deformable secondary mirror under different atmospheric coherence length (r0) conditions.

For the optical imaging system, the contrast of the imaging results is closely related to the SR of the point spread function of the imaging system. The higher the SR of the imaging system

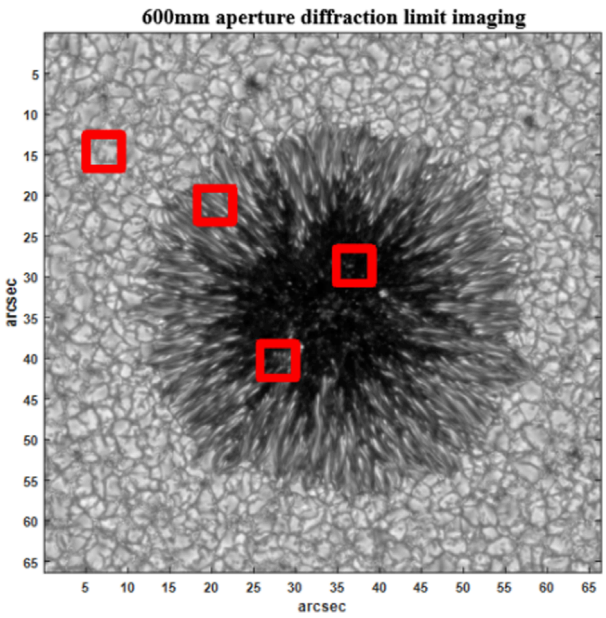

FIGURE 5
Target image that was used for simulation experiments.

is, the better the quality of the imaging results, the higher the contrast, and the clearer the discernible image details will be. Since image degradation is closely related to the residual aberration of the system, the simulation of system imaging is also carried out according to the real imaging process. In order to obtain the degenerative effects of different regions of a typical solar photosphere image with different correction capabilities, we selected a simulated solar image containing sunspot umbra, penumbra, and granulations, as shown in Figure 5. This image corresponds to the sunspot run presented in Rempel (2012), which was computed with the MURaM code (Vögler et al., 2005), and the simulation run is also publicly available (https://download.hao.ucar.edu/pub/rempel/sunspot_models/). The original simulated image has a total of 4,000 × 4,000 pixels, with a pixel resolution of 0.0166″, corresponding to a pixel size of 12 km. The simulated atmospheric turbulence distribution follows the Kolmogorov spectrum, where the atmospheric turbulence condition is D/r0 = 10, and in order to obtain the imaging results of different Strehl ratios, a variety of residual aberration conditions are obtained by setting different AO system correction capabilities. The residual aberration of the corrected system is used to calculate the corresponding PSF, and the degraded image is obtained by the convolution of the PSF and the original target image (Wöger, 2010). After that, the convolution of the point spread function and the diffraction-limited image of the 60 cm telescope were used to obtain the degraded image with different correction capabilities. The contrast of different regions of the degraded image was calculated to show the influence of the correction ability on the imaging system.

By simulating the situation of different atmospheric turbulence disturbances and different correction capabilities of the adaptive optics systems, the contrast of solar granulation and sunspots can be directly improved by enhancing the SR of the imaging system. Figure 6 shows the overall differential comparison of the different image qualities for the same solar target when the SR is gradually increased from 0.03 to 0.9. Figure 7 illustrates the differential comparison of the local details of solar granulation and sunspots under different SR conditions.

According to the simulation results, to obtain imaging results with high contrast and rich details, the solar telescope needs to be equipped with an advanced adaptive optics correction system. Only if the imaging system SR ≥ 0.5, the details between the solar granulation, especially between the sunspot internal, can be clearly identified. This also presents higher demands for the development of instrumental equipment. Achieving near-diffraction-limited imaging resolution in solar observation images while maintaining high SR at the same time is crucial for ensuring high measurement accuracy of the instrument, and this will provide more accurate measurement data for cutting-edge solar physics research.

Based on simulation experiments, the correction field of this instrument for high-order CAO is approximately 10″-20″ and that for large-filed GLAO imaging is around 2'. To achieve high-resolution imaging with an 8′ full FoV, post-processing techniques for image reconstruction must be employed. On the other hand, one important scientific objective of this equipment is to obtain high photometric accuracy and high-resolution images, particularly for the post-processing of Fe I magnetic field channel measurement data. This not only requires reconstruction algorithms to effectively improve image resolution but also requires the physical reality and light intensity reality of the reconstructed images. Phase diversity (PD) image reconstruction is to simultaneously collect one or more sets of images of the same target through different optical channels and reconstruct a clear target based on the measurement of the wavefront aberration that causes image distortion (Gonsalves, 1982; Löfdahl and Scharmer, 1994; Thelen et al., 2009; Löfdahl and Hillberg, 2022). Therefore, the PD image reconstruction method is a type of image reconstruction based on optical measurement, and its algorithm principle can ensure high photometric accuracy of the reconstructed results. We use a camera exposure external trigger control circuit to simultaneously capture the focus and defocus images and reconstruct a clear image from a degraded target based on accurate wavefront detection. On this basis, we can ensure image restoration with a large FoV and high photometric accuracy. Further research and experimental verification will be conducted in the future.

5 Conclusion and remarks

This paper reports a novel solar adaptive telescope, PASAT, and the systematic design and performance evaluation are also presented. The PASAT is planned to be put into operation in 2026 and built at the Wumingshan Observation Station in Daocheng, Sichuan, China, which has good meteorological conditions. After years of site selection, the Daocheng Wuming Mountain at an altitude of 4,800 m was chosen because it has natural advantages such as low atmospheric scattered light, an average daytime r0 value of 7.65 cm, and approximately

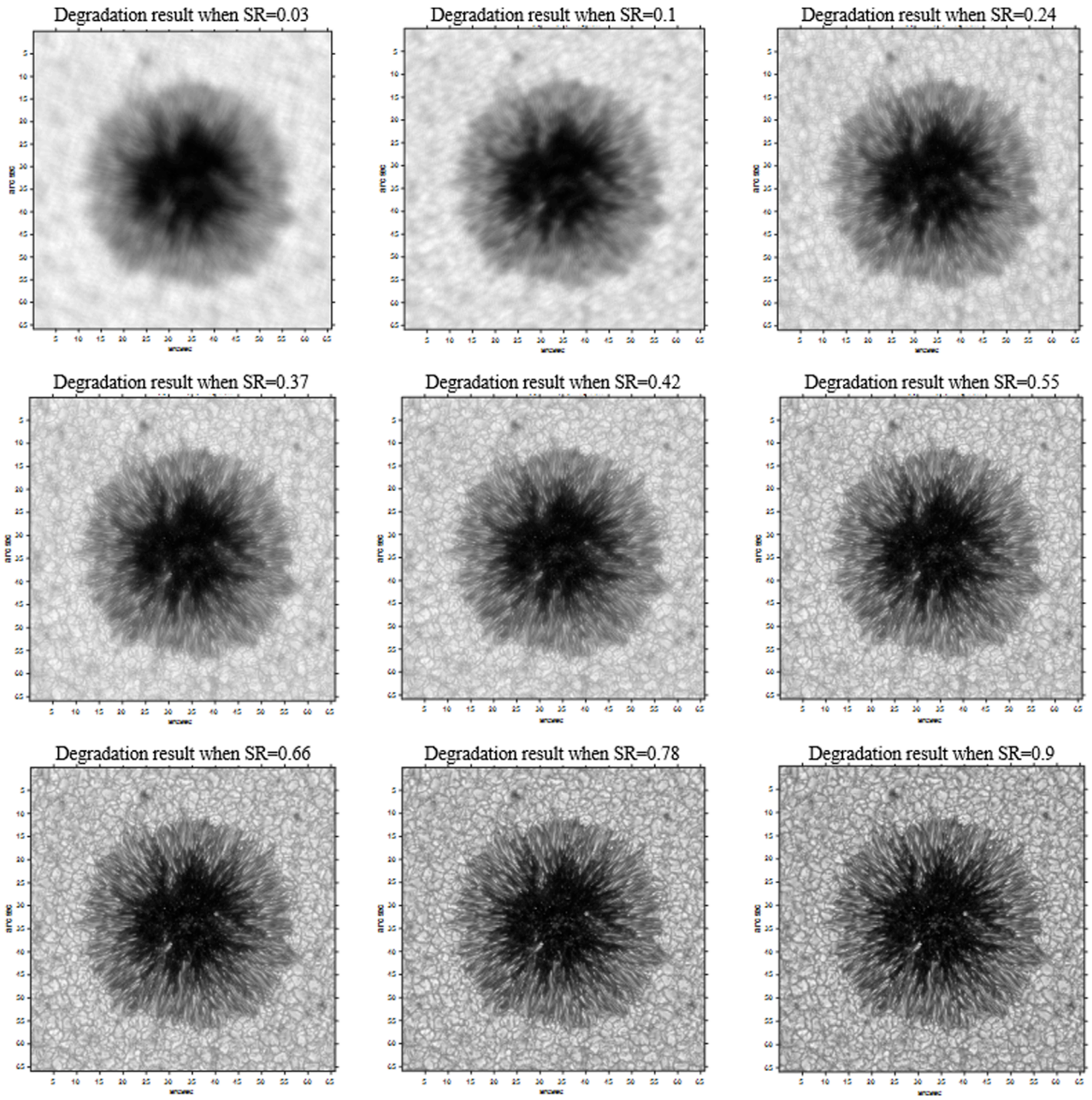

FIGURE 6
Degradation of the target by the point spread function under different Strehl ratios. From the graph in a large field of view of approximately 1′, it can be seen through an intuitive comparison that a higher Strehl ratio can retain more details and significantly improve the imaging resolution. Referring to the PASAT technical parameters, when the Strehl ratio is 0.4@ r0 (0.50 μm) = 6 cm, the imaging system can ensure that the results contain relatively complete, fine, and clear structures.

250 available sunny days throughout the year (Song et al., 2020). Many telescopes, such as the 2.5 m WeHoST, are planned to be placed at this station. After the completion of PASAT, it will become the first high-resolution magnetic field measurement solar-adaptive telescope without calibration units in the world.

The biggest technological innovation of this instrument is that it uses the simplest optical path to obtain richer deep-level image information while ensuring a certain degree of high spatial resolution and pursuing the ultimate image signal–noise ratio (SNR) and photometric accuracy. It can provide high-quality data support for space weather forecasting and early warning applications.

More importantly, PASAT provides an exploration of a new large solar telescope with the capability of high-contrast imaging as the pathfinder. Its accumulated relevant techniques can be applied to the construction of similar, larger solar telescopes in the future.

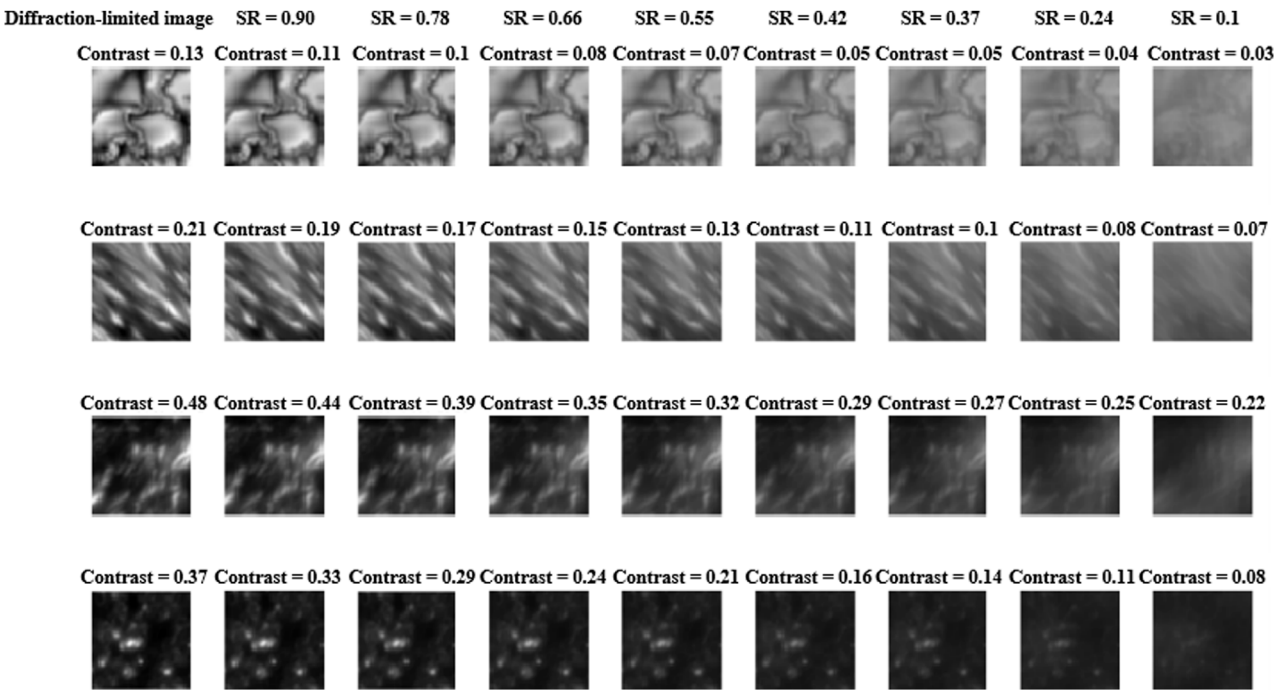

FIGURE 7
Contrast of the different regions (granulation, penumbra, and umbra, from top to bottom) as the Strehl ratio changes. It can be seen that the higher the Strehl ratio (from right to left), the better the correction effect of the system, and the higher the contrast of each sub-region. The size of the sub-region is 256 × 256 pixels, with a pixel resolution of 0.016″ and a corresponding field of view of approximately 4". Referring to the PASAT technical parameters, when the Strehl ratio is 0.4@ r0 (0.50 μm) = 6 cm, the contrast of granulation, penumbra, and umbra is larger than 5%, 11%, and 16%, respectively.

Data availability statement

The raw data supporting the conclusion of this article will be made available by the authors, without undue reservation.

Author contributions

CR: writing–review and editing, writing–original draft, visualization, validation, supervision, software, resources, project administration, methodology, investigation, funding acquisition, formal analysis, data curation, and conceptualization. HJ: writing–review and editing, visualization, validation, supervision, software, resources, project administration, methodology, investigation, funding acquisition, formal analysis, data curation, and conceptualization. HB: writing–review and editing, visualization, validation, supervision, software, resources, project administration, methodology, investigation, funding acquisition, formal analysis, data curation, and conceptualization. XR: writing–review and editing, formal analysis, data curation, and conceptualization. JY: writing–review and editing, formal analysis, data curation, and conceptualization. YG: writing–review and editing, investigation, data curation, and conceptualization. LaZ: writing–review and editing, investigation, data curation, and conceptualization. LiZ: writing–review and editing, data curation, and conceptualization. XF: writing–review and editing, data curation, and conceptualization. QZ: writing–review and editing, validation, investigation, data curation, and conceptualization. CL: writing–review and editing, investigation, data curation, and conceptualization. QB: writing–review and editing, validation, investigation, formal analysis, data curation, and conceptualization.

Funding

The author(s) declare that financial support was received for the research, authorship, and/or publication of this article. This work is funded by the National Natural Science Foundation of China (No. 12261131508) and the Laboratory Innovation Foundation of the Chinese Academy of Science (No. YJ22K002).

Acknowledgments

The authors would like to particularly thank Professor Pengfei Chen at Nanjing University for many helpful discussions and suggestions, and sincerely thank CAS Nanjing Astronomical Instruments Co., LTD for providing the polar axis frame design scheme and corresponding schematic diagram for this project.

Conflict of interest

The authors declare that the research was conducted in the absence of any commercial or financial relationships that could be construed as a potential conflict of interest.

Publisher's note

References

Briguglio, R., Quirós-Pacheco, F., Males, J. R., Xompero, M., Riccardi, A., Close, L. M., et al. (2018). Optical calibration and performance of the adaptive secondary mirror at the Magellan telescope. *Sci. Rep.* 8, 10835. doi:10.1038/s41598-018-29171-6

Briguglio, R., Xompero, M., Riccardi, A., Andrighettoni, M., Pescoller, D., Roberto, B., et al. (2013). "Optical calibration and test of the VLT deformable secondary mirror," in Proceedings of the Third AO4ELT Conference, Florence, Italy, 26-31 May 2013. doi:10.12839/AO4ELT3.13507

Cao, W., Gorceix, N., Coulter, R., Ahn, K., Rimmele, T. R., and Goode, P. R. (2010). Scientific instrumentation for the 1.6 m new solar telescope in big bear. *Astron. Nachr.* 331 (6), 636–639. doi:10.1002/asna.201011390

Choudhuri, A. R. (2017). Starspots, stellar cycles and stellar flares: lessons from solar dynamo models. *Sci. China Phys. Mech. Astron* 60, 019601. doi:10.1007/s11433-016-0413-7

Esposito, S., Riccardi, A., Pinna, E., Puglisi, A., Quirós-Pacheco, F., Arcidiacono, C., et al. (2011). Large binocular telescope adaptive optics system: new achievements and perspectives in adaptive optics. *Proc. SPIE* 8149, 814902. doi:10.1117/12.898641

Fang, C., Gu, B. Z., Yuan, X. Y., Ding, M. D., Chen, P. F., Dai, Z. G., et al. (2019). 2.5 m wide-field and high-resolution telescope. *Sci. China Phys. Mech. Astron.* 49 (5), 059603. doi:10.1360/SSPMA2018-00313

Gonsalves, R. A. (1982). Phase retrieval and diversity in adaptive optics. *Opt. Eng.* 21 (5), 829–832. doi:10.1117/12.7972989

Guo, Y. M., Chen, K. L., Zhou, J. H., Li, Z. D., Han, W. Y., Rao, X. J., et al. (2023). High-resolution visible imaging with piezoelectric deformable secondary mirror: experimental results at the 1.8-m adaptive telescope. *Opto-Electron Adv.* 6 (12), 230039. doi:10.29026/oea.2023.230039

Guo, Y. M., Zhang, A., Fan, X. L., Rao, C. H., Wei, L., Xian, H., et al. (2016a). First on-sky demonstration of the piezoelectric adaptive secondary mirror. *Opt. Lett.* 41 (24), 5712–5715. doi:10.1364/OL.41.005712

Guo, Y. M., Zhang, A., Fan, X. L., Rao, C. H., Wei, L., Xian, H., et al. (2016b). First light of the deformable secondary mirror-based adaptive optics system on 1.8m telescope. *Proc. SPIE* 9909, 99091D. doi:10.1117/12.2231842

Hardy, J. W., and Thompson, L. (2000). Adaptive optics for astronomical telescopes. *Phys. Today* 53 (4), 69. doi:10.1063/1.883053

Kleint, L., Berkefeld, T., Esteves, M., Sonner, T., Volkmer, R., Gerber, K., et al. (2020). GREGOR: optics redesign and updates from 2018-2020. *Astron. Astrophys.* 641, A27. doi:10.1051/0004-6361/202038208

Liu, Z., Xu, J., Gu, B. Z., Wang, S., You, J. Q., Shen, L. X., et al. (2014). New vacuum solar telescope and observations with high resolution. *Res. Astron. Astrophys.* 14 (6), 705–718. doi:10.1088/1674-4527/14/6/009

Löfdahl, M. G., and Hillberg, T. (2022). Multi-frame blind deconvolution and phase diversity with statistical inclusion of uncorrected high-order modes. Available at: https://arxiv.org/abs/2205.13650 (Accessed October 31, 2022).

Löfdahl, M. G., and Scharmer, G. B. (1994). Wavefront sensing and image restoration from focused and defocused solar images. *Astronomy Astrophysics Suppl* 107 (2), 243–264. doi:10.1086/117172

Low, B. C. (2015). Field topologies in ideal and near-ideal magnetohydrodynamics and vortex dynamics. *Sci. China Phys. Mech. Astron.* 58, 1–20. doi:10.1007/s11433-014-5626-7

Morzinski, K. M., Close, L. M., Males, J. R., Kopon, D., Hinz, P. M., Esposito, S., et al. (2014). MagAO: status and on-sky performance of the Magellan adaptive optics system. *Proc. SPIE* 9148, 914804. doi:10.1117/12.2057048

Rao, C. H., Gu, N. T., Rao, X. J., Li, C., Zhang, L. Q., Huang, J. L., et al. (2020). First light of the 1.8-m solar telescope–CLST. *Sci. China Phys. Mech. Astron* 63, 109631. doi:10.1007/s11433-019-1557-3

Rao, C. H., Rao, X. J., Du, Z. M., Bao, H., Li, C., Huang, J. L., et al. (2022). EAST-educational adaptive-optics solar telescope. *Res. Astron. Astrophys.* 22, 065003. doi:10.1088/1674-4527/ac65e8

Rao, C. H., Zhang, L. Q., Kong, L., Guo, Y. M., Rao, X. J., Bao, H., et al. (2018). First light of solar multi-conjugate adaptive optics at the 1-m new vacuum solar telescope. *Sci. China-Phys. Mech. Astron.* 61, 089621. doi:10.1007/s11433-017-9178-6

Rao, C. H., Zhu, L., Rao, X. J., Guan, C. L., Chen, D. H., Lin, J., et al. (2010). 基于云南天文台26厘米太阳精细结构望远镜的37单元太阳自适应光学系统. *Chin. Opt. Lett.* 8 (10), 966–968. doi:10.3788/COL20100810.0966

Rast, M. P., Bello González, N., Rubio, L. B., Cao, W., Cauzzi, G., DeLuca, E., et al. (2021). Critical science plan for the Daniel K. Inouye solar telescope (DKIST). *Sol. Phy.* 296, 70. doi:10.1007/s11207-021-01789-2

Rimmele, T. R., and Marino, J. (2011). Solar adaptive optics. *Living Rev. Sol. Phys.* 8, 2. doi:10.12942/lrsp-2011-2

Rimmele, T. R., Richards, K., Hegwer, S., Fletcher, S., Gregory, S., Moretto, G., et al. (2004). First results from the NSO/NJIT solar adaptive optics system. *Proc. SPIE.* 5171, 179. doi:10.1117/12.508513

Rimmele, T. R., Warner, M., Keil, S. L., Goode, P. R., Knölker, M., Kuhn, J. R., et al. (2020). The Daniel K. Inouye.solar telescope – observatory overview. *Sol. Phys.* 295, 172. doi:10.1007/s11207-020-01736-7

Scharmer, G. B., Bjelksjo, K., Korhonen, T. K., Lindberg, B., and Petterson, B. (2002). The 1-meter Swedish solar telescope. *Proc. SPIE.* 4853, 47. doi:10.1117/12.460377

Schmidt, D., Gorceix, N., Goode, P. R., Marino, J., Rimmele, T., Berkkefeld, T., et al. (2017). Clear widens the field for observations of the Sun with multi-conjugate adaptive optics. *Astron. Astrophys.* 597, L8. doi:10.1051/0004-6361/201629970

Schmidt, D., Gorceix, N., Marino, J., Berkefeld, T., Rimmele, T., Zhang, X. Y., et al. (2016). Progress in multi-conjugate adaptive optics at big bear solar observatory. *Proc. SPIE.* 9909, 1. doi:10.1117/12.2232087

Schmidt, W., Von der Lühe, O., Volkmer, R., Denker, C., Solanki, S. K., Balthasar, H., et al. (2012). The 1.5 meter solar telescope GREGOR. *Astron. Nachrichten* 333 (9), 796–809. doi:10.1002/asna.201211725

Shumko, S., Gorceix, N., Choi, S., Kellerer, A., Cao, W., Goode, P. R., et al. (2014). AO-308: the high-order adaptive optics system at Big Bear Solar Observatory. *Proc. SPIE.* 9148, 914835. doi:10.1117/12.2056731

Soltau, D., Berkefeld, T., Sánchez Capuchino, J., Collados Vera, M., Del Moro, D., Löfdahl, M., et al. (2010). Adaptive optics and MCAO for the 4-m European solar telescope EST. *Proc. SPIE.* 7736, 77360U. doi:10.1117/12.856851

Song, T. F., Liu, Y., Wang, J. X., Zhang, X. F., Liu, S. Q., Zhao, M. Y., et al. (2020). Site testing campaign for the Large Optical/infrared Telescope of China: general introduction of the Daocheng site. *Res. Astron. Astrophys.* 20 (6), 085. doi:10.1088/1674-4527/20/6/85

Thelen, B. J., Paxman, R. G., Carrara, D. A., and Seldin, J. H. (2009). Overcoming turbulence-induced space-variant blur by using phase-diverse speckle. *J. Opt. Soc. Am. A* 26 (1), 206–218. doi:10.1364/JOSAA.26.000206

Wang, J. X., Zhang, Y. Z., He, H., Chen, A. Q., Jin, C. L., and Zhou, G. P. (2015). Cluster of solar active regions and onset of coronal mass ejections. *Sci. China Phys. Mech. Astron.* 58, 599601. doi:10.1007/s11433-015-5682-7

Wei, X. Y., Noda, C., Zhang, L. Q., and Rao, C. H. (2023). Comparative analysis of image-shift measurement algorithms for solar shack–hartmann wavefront sensors. *Publ. Astronomical Soc. Pac.* 135, 114503. doi:10.1088/1538-3873/ad0451

Wildi, F. P., Brusa, G., Lloyd-Hart, M., Close, L. M., and Riccardi, A. (2003). First light of the 6.5-m MMT adaptive optics system. *Proc. SPIE* 5169, 17–25. doi:10.1117/12.507687

Wöger, F. (2010). Optical transfer functions derived from solar adaptive optics system data. *Appl. Opt.* 49 (10), 1818–1825. doi:10.1364/AO.49.001818

Zhang, L. Q., Bao, H., Rao, X. J., Guo, Y. M., Zhong, L. B., Ran, X., et al. (2023). Ground-layer adaptive optics for the new vacuum solar telescope:instrument description and first results. *Sci. CHINA-PHYSICS Mech. ASTRONOMY* 6, 200–210. doi:10.1007/s11433-022-2107-4